Research Article   **Open Access**

Non-contact Deep Tissue Imaging using a Hand-Held Near-infrared Optical Scanner

Young-Jin Jung, Manuela Roman, Jennifer Carrasquilla, Sarah J Erickson and Anuradha Godavarty*

Department of Biomedical Engineering, Florida International University, Optical Imaging Laboratory, EC 3365, Miami, FL 33174, USA

*Corresponding author: Anuradha G, Florida International University, 10555 West Flagler Street EC 2675, Miami, Florida 33174, USA, Tel: +1 (305) 348-7340; Fax: +1 (305) 348-6954; E-mail: godavart@fiu.edu

Abstract

Fiber-free non-contact near-infrared (NIR) imaging devices using wide-field detectors are emerging apart from the contact and fiber-based NIR devices. Unlike the fiber-based devices that can image deep tissues, the fiber-free non-contact devices have been used only for subsurface imaging (≤ 1 cm) to date. A new compact ($7 \times 8 \times 12$ cm^3) hand-held Near-Infrared. Optical Scanner (NIROS) has been developed for fiber-free non-contact imaging of deep tissues in both reflectance and transmittance modes. Absorption-contrasted diffuse imaging studies were performed on tissue mimicking cubical phantoms ($5.5 \times 5.5 \times 5.5$ cm^3 volume) using India. Ink based targets located at various depths (0.5 to 4 cm) in both reflectance and transmittance modes. Preliminary *in vivo* breast imaging studies in transmittance mode were also performed to determine the deep target detectability of NIROS. The hand-held NIROS could detect targets up to 1.5 cm in reflectance mode and across the entire depth of the phantom (4 cm deep) in transmittance mode, as observed from phantom studies. Absorption-contrasted targets placed as deep as 6 cm were detectable *in vivo* breast tissues during transmittance imaging, when comfortable pressure was applied via compression. The non-contact hand-held NIROS demonstrated the ability to detect targets deeper than 1 cm (which was the limit attempted to date using other non-contact NIR devices in phantoms or *in vivo*). The ability of the portable handheld NIROS to perform deep tissue imaging can allow for *in vivo* breast imaging studies in the future, with a potential as an initial assessment tool for breast cancer pre-screening.

Keywords: Near-infrared; Diffuse optical imaging; Hand-held; Optical scanner; Non-contact; Deep tissues; Breast

Introduction

Over the past 30 years, near-infrared (NIR) optical imaging approaches have been developed for deep tissue breast cancer imaging, sub-surface skin monitoring, imaging blood vessel, and various other applications based upon the endogenous absorption contrast owing to the changes in the blood flow concentrations across the different tissue types. The NIR light (700-900 nm) for is minimally absorbed and preferentially scattered, allowing its propagation through deep tissues. NIR-based optical imager can be broadly categorized into bed-side [1-3], hand-held [4,5], and parallel-plate based imagers [6,7] (selected references). Both the bed-based and parallel-plate based imagers were developed for three-dimensional (3D) tomographic imaging of deep tissues (e.g. breast), where the tissue is compressed in parallel-plate imagers alone. On the contrary, hand-held optical imagers, which employ a surface reflectance-based imaging configuration, are developed for two-dimensional (2D) spectroscopic imaging of the tissues [4,5]. All the bed-based and parallel-plate imagers and most of hand-held imagers available to date employ optical fibers to illuminate/detect NIR signals. The use of optical fibers allows precise launching and collection of NIR optical signals at point locations on the tissue surface. The intensity and location of these source and detector points using optical fibers when measured allows 3D tomographic imaging. However, the use of optical fibers can also be disadvantageous. The differences in the length across multiple optical fibers in imaging systems can cause variability in the launched or detected intensity signals. Many optical fibers or fiber bundles are required to enhance the spatial resolution of the imaging system, but at the cost of increased bulkiness, reduced flexibility (especially in hand-held devices), and instrumentation expense. Additionally, optical-fiber based devices are effective for only contact-based imaging and hence may be limited to imaging closed tissues and not any open wounds (e.g. ulcerations, surgical site etc.).

In recent years, a few research groups have developed fiber-free NIR imaging systems using wide-field detectors (e.g. CCD or CMOS camera) for non-contact imaging. The various fiberfree non-contact NIR imagers available to date are provided in Table 1 [8-27]. These imagers employ either reflectance or transmittance mode to image tissue phantoms, blood vessels, and/or veins of the skin surface. While most of these non-contact imagers are bench-top, those developed by Bouzida et al. [14] and Liu et al. [23] were hand-held transmittance based devices to image veins (with no contrast agent) and sentinel lymph node mapping (using fluorescence contrast agent, ICG), respectively. Unlike the fiber-based devices (with contact) that can image deep tissues, all the fiber-free non-contact devices have been used for sub-surface imaging (Table 1). The maximum detectable target depth of the fiber-free NIR device attempted to date was ≤ 1 cm and not deeper targets. Detection of deep targets (>1 cm) can expand the potential of these non-contact devices to other applications such as breast cancer imaging.

Ref (year)	Imaging Modality	Source	Detector	Absorption/Fluoresce contrast agent	Target tissue	Target depth	Imaging Resolution (area)	Hand Held
Palmer et al. (2002) [8]	Reflectance	450 W XeArc Lamp 630/755 nm	CCD	Fluorescence (ICG)	CSF*/Vein	0~10 mm	1280 × 1024	/
Wieringa et al. (2006) [9]	Reflectance	LED 910-920 nm	CMOS	N/A	Blood vessel	Surface	320 × 256	No
Han et al. (2006, 2009) [10,12]	Reflectance	Laser Diode 785 nm	CCD	Fluorescence	Skin	Surface	768 × 512 (25 mm Diameter circle)	/
Matsushita et al. (2007, 2011) [11,21]	Reflectance	LED 700 /810 nm	CCD	N/A	Surface vessels	5 mm	/	No
Abookasis et al. (2009) [13]	Reflectance	White Mercury Lamp	CCD	N/A	Rat Brain	Surface	512 × 512	No
Bouzida et al. (2010) [14]	Trans-illumination	LED 859-940 nm	CCD	N/A	Hand veins	0~10 mm	/	/
Mizuno et al. (2010) [15]	Trans-illumination	LED 700/1000 nm (human) 660/805/880 nm (Phantom)	CMOS	N/A	Blood Vessel	0~10 mm	/	No
Lee et al. (2010) [16]	Reflectance	LED 400-650 nm, 745-779 nm	CCD	Fluorescence (ICG)	Tissue surface	Surface	/	No
Chen et al. (2010) [17]	Trans-illumination	LED 940 nm	CMOS	N/A	Blood Vessel	0~10 mm	/	No
Jakovels et al. (2010) [18]	Reflectance	LED white	CCD	N/A	Skin hemoglobin and melanin	Surface	/	No
Shao et al. (2010) [19]	Reflectance	Laser diode 785 nm and Tungsten halogen light	CCD	(auto-fluorescence)	Colonic Cancer	surface	512 × 512	No
Shimawak i et al. (2010) [20]	Trans-illumination	LED 850 nm	CCD	N/A	Blood Vessel	0~10 mm	/	No
Lin et al. (2011) [22]	Reflectance	Laser diode 808 nm	CCD	none	Tissue phantom	6.5 mm	496 × 656 (13 × 11 mm^2)	No
Liu et al. (2011) [23]	Reflectance	LED white/770 nm	CCD	Fluorescence (ICG)	Sentinel lymph node	surface	30 cm in diameter	Yes
Mieog et al. (2011) [24,25]	Reflectance	LED 700/830 nm	CCD	Fluoresce (ICG)	Breast cancer	0~10 mm	/	No
Kuzmin et al. (2011) [26]	Reflectance	LED 450-950 nm White	CCD	N/A	Hand skin	Surface	/	No
Osaki et al. (2011) [27]	Reflectance	Laser diode 980 nm	CCD	Fluoresce (RED-CNP: Red-Earth-Doped Ceramic NanoPhosphors)	Phantom and chicken Breast tissue	0~10 mm	/	No

Table 1: Summary of different fiber-free non-contact devices for NIR imaging. *CSF: Cerebrospinal Fluid, /: Unknown, ICG : Indocyanine green, CMOS : Complementary metal-oxide-semiconductor, CCD: Charge-coupled device, LED : Light-emitting diode.

In the current work, a fiber-free non-contact based hand-held near-infrared optical scanner (NIROS) has been developed towards deep tissue imaging (>1 cm target depth) in both reflectance and transmittance mode. The details of the scanner and the associated software (developed as a Matlab based graphical user interface) are described. Tissue phantom studies were performed on cubical phantoms containing absorption targets (0.5-4 cm deep), via reflectance and transmittance imaging. Preliminary *in vivo* breast imaging studies as a noncontact device was also performed to determine the deep target detectability of the scanner.

Materials and Methods

Instrumentation

The fiber-free non-contact hand-held NIR optical scanner (NIROS) is comprised of a hand-held probe, a controller box, and a computer (Figure 1) with custom-developed image acquisition/processing toolbox (Figure 2).
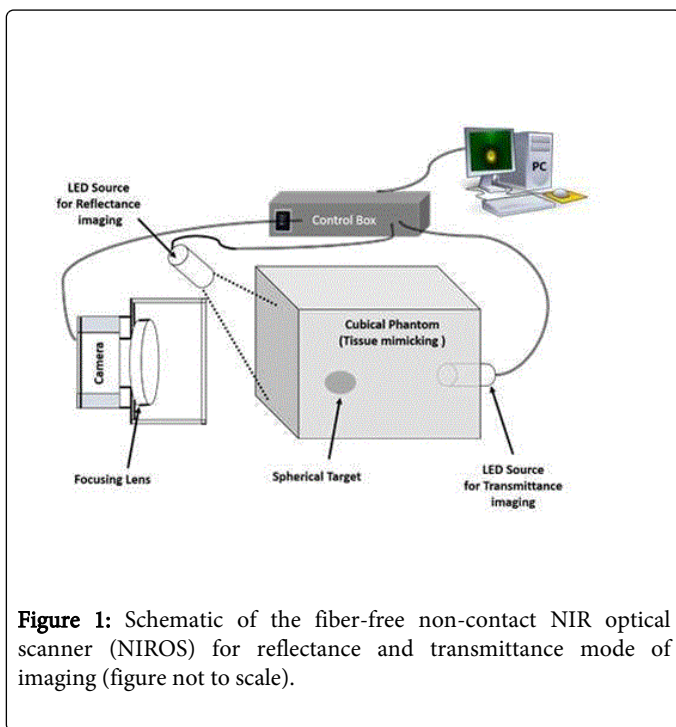
Figure 1: Schematic of the fiber-free non-contact NIR optical scanner (NIROS) for reflectance and transmittance mode of imaging (figure not to scale).
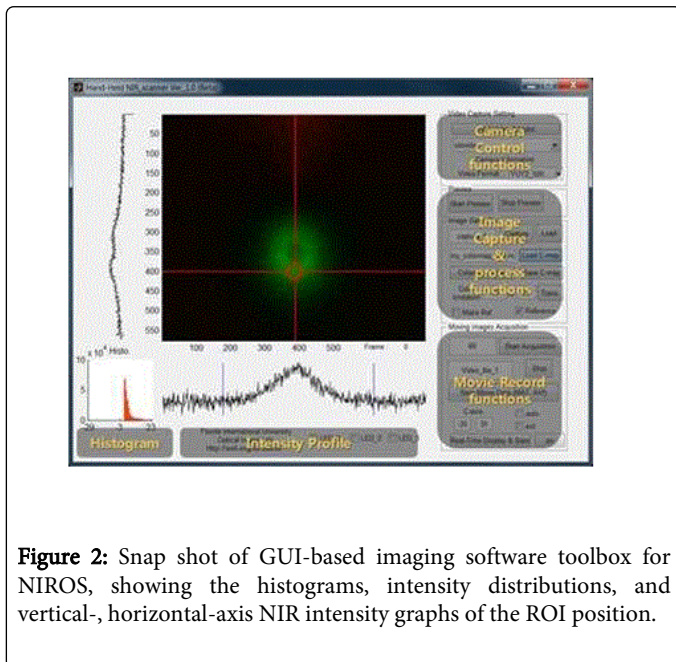
Figure 2: Snap shot of GUI-based imaging software toolbox for NIROS, showing the histograms, intensity distributions, and vertical-, horizontal-axis NIR intensity graphs of the ROI position.

Hand-held Probe of NIROS

The hand-held probe ($7 \times 8 \times 12$ cm^3 housing and entire size: <0.019 m^3) of NIROS is compactly designed for comfortable and light-weight grip in the hand. The probe consists of a 780 nm LED-based light source (of maximum power of 50 mw) that launches NIR light via area illumination, and an analog CCD camera (Xc-E150CE, Sony, Japan) coupled with a focusing lens that acquires the attenuated NIR signal via area detection (~12 cm^2 area). This interline CCD camera is NIR sensitive with a signal-to-noise ratio of 60 db. The CCD camera acts as a fiber-free wide-field detector with a spatial resolution of 752×582 pixels. The acquired analog signal from the CCD sensor is transferred to the camera adaptor (DC-700/700CE, Sony, Japan), which is placed in the controller box along with the LED driver system. The detected analog signal is digitized using a frame grabber (DT3120, Data-Translation Inc. USA) installed in the computer. The LED source's radiation power was stabilized (5 minutes after turning ON the source) and maintained at a constant value via the LED driver during the CW-imaging studies. The hand-held probe also has an in-built optical filter slot that allows the use of appropriate optical filters for diffuse optical imaging studies (and fluorescence studies in the future).

GUI-based Imaging Software of NIROS

A graphical user interface (GUI) based imaging software was developed in-house using Matlab (Ver. 2009[b] with image acquisition toolbox) to conveniently control the scanner for real-time acquisition of the NIR intensity images (Figure 2). The developed GUI toolbox consisted of three function blocks: (i) camera control, (ii) image capture and process, and (iii) video/movie recordings. The detector can record dynamic images at a maximum of 30 frames/sec. When subtracted imaging (i.e. subtracting background image from the images containing targets) is performed, the overall computational time increases due to increase in data processing time between image acquisition times (at 30 frames/sec). The developed imaging software allows image processing via various in-built functions in the GUI. These functions include histogram of the intensity distribution in the displayed image, region of interest (ROI) positioning, and intensity profiles along each axis of the 2D images (at any ROI). These features are automated in the imaging software such that the data analysis time is reduced.

Experimental Study

The capability of the fiber-free hand-held NIROS to perform deep tissue imaging via reflectance and transmittance imaging modes has been demonstrated via tissue-mimicking phantom studies. Cubical phantoms of $5.5 \times 5.5 \times 5.5$ cm^3 volume were filled with 45% organic milk as the background during the continuous-wave (CW) based imaging studies. The 45% organic milk was utilized to mimic the optical properties of human tissue. The background optical properties of the phantom (filled with 45% organic milk) were measured in the laboratory (via a homodyne frequency domain based optical imaging system) as absorption coefficient, $\mu a=0.069$ cm^{-1}, and reduced scattering coefficient, $\mu s'=7.36$ cm^{-1}. Spherical target(s) (of 0.23 cc volume) filled with 0.8% India Ink (absorbing agent: Chartpak, Leeds, MA) were used as tumor mimicking objects, with optical properties different from that of the background (here, higher absorption from the background). The target(s) were placed at various depths of 0.5 to 4 cm (at 0.5 cm increments) from the detection surface and studies

were performed in reflectance and transmittance imaging modes (Figure 3). During reflectance imaging studies, the NIR light source (780 nm LED) and the CCD-detector were placed on the same surface as shown in Figure 3 (mode #2: reflectance mode). The maximum radiated NIR light on the phantom surface was 2.24 mw, as the light source was not in contact to the phantom surface in order to illuminate and detect the same region of interest (here, 12 cm). Hence, the optical power dropped to 2.24 mw on the illuminating phantom surface, as the LED source had to be placed away from the field of view of the camera, and still illuminate the same region of interest that is detected. During transmittance imaging studies, the LED light source was placed on the opposite surface from the detected plane as shown in figure (mode #1: transmittance mode). Here, the maximum radiated NIR light on the illuminating surface was high (45 mw) as the source was not in the field of view of the detector, and hence could be placed closer to the surface. The LED source was located at the center of the illuminating plane during transmittance imaging.
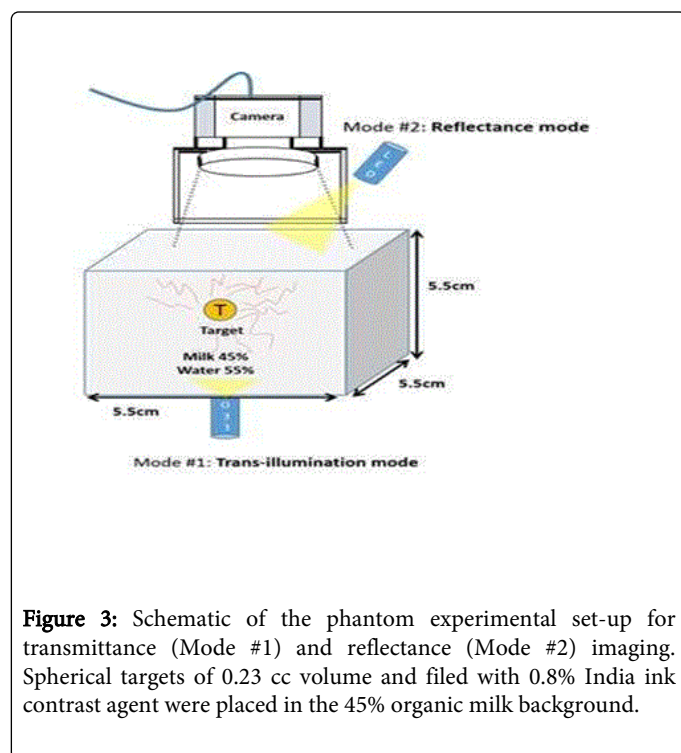
Figure 3: Schematic of the phantom experimental set-up for transmittance (Mode #1) and reflectance (Mode #2) imaging. Spherical targets of 0.23 cc volume and filed with 0.8% India ink contrast agent were placed in the 45% organic milk background.

Imaging and Data Processing

The original NIR intensity data was acquired via non-contact area imaging (~12 cm^2) using the CCD camera. The total pixelated amplitude intensity data (from 752×582 pixels) included the meaningful NIR signals from the phantom depths, electrical noise, and systemic error signals. In order to account for the instrument effects and improve the optical contrast for detection of deep targets, a few post-image processing approaches were employed. These include median filter, subtraction technique, histogram stretching. The median filtering, a nonlinear spatial digital filtering technique, is widely used to reduce noise in an image, particularly "salt and pepper noise," commonly seen on images [28]. In the current study, median filtering with (3×3) box pattern windows was employed to remove the noise (which is dark pixels in bright regions and bright pixels in dark region on the measured image). The subtraction technique was implemented wherein NIR images obtained from the phantoms containing target(s) were subtracted from NIR images obtained from the phantoms without target(s) (i.e. background subtraction was performed).

The detected target position was estimated using a histogram thresholding technique, based on histogram density [29]. A balanced histogram thresholding is a simple approach that can be used for automatic image segmentation [30-32]. However, there is lack of a distinct boundary that differentiates the target from the background from the surface NIR images (in spite of employing the subtraction technique). Hence, an empirical histogram threshold criterion was employed, wherein the bottom 5% of the subtracted NIR intensity values were used as a threshold level to differentiate the target from the background. The target position (centroid location and radius) was calculated from the segmented area using thresholding process (using in-built Matlab functions). Finally, the "distance off" was calculated as the distance between true target location and estimated target's 2D centroid location in order to determine the accuracy of target localization from 2D imaging studies. The thresholding technique is applicable when the background is homogeneous as in phantoms, and may not be appropriate for heterogeneous tissues. Hence, this technique was not applied to preliminary *in vivo* studies. Image contrast can be used as a major factor to distinguish target from background and it can be a good index to estimate the image quality for segmentation of the subtracted NIR intensity image. In this study, the root mean square (RMS) contrast estimator was adopted to estimate the contrast of subtracted NIR image. It is based on the standard deviation of the NIR intensities, as shown in equation (1).

$$RMS_{contrast X} = \sqrt{\frac{\Sigma_{i=1}^{N} \Sigma_{j=1}^{M} (Iij - \bar{I})^2}{M \times N}} \qquad (1)$$

where Σ is a grey-level value ($0 \leq I \leq 1$) of a subtracted NIR intensity and Iij is the ith and jth elements of the measured 2D NIR image. Image size is represented by $M \times N$ matrix. $\bar{}$ is the mean intensity value of the (entire) subtracted NIR image. The RMS contrast does not depend on spatial frequency content or the spatial distribution of contrast in the image [33]. Here, the nonnormalized NIR intensity value was used instead of the normalized data (as typically used by other researchers when estimating the RMS contrast) in order to include the effect of absolute intensity value difference that preserves the actual properties of the acquired image. In addition, the contrast was also estimated as the absolute difference between the maximum and minimum intensity values in the subtracted imaged region. Figure 4 shows the raw NIR intensity data in comparison to the processed data using the above data processing techniques. The experimental data shown as an example case is a transmittance imaging case where a 0.23 cc target was located 1 cm deep from the detection plane. The spherical target was not differentiable from the background in the raw NIR data (Figure 4(A)). There was strong transmitted and scattered intensity distribution pattern generated from the LED (45 mw) source located on the opposite side of the detection plane. This background (source) noise pattern was significantly reduced upon implementing the subtraction technique (Figure 4(B)). The target boundary was better differentiated by employing the 5% threshold level (Figure 4(C)). The target position and radius (dotted red line in the Figure 4(D)) was further estimated (automatically) using the extracted target area. The data post-processing techniques were implemented in Matlab as distinct from the real-time GUI software.
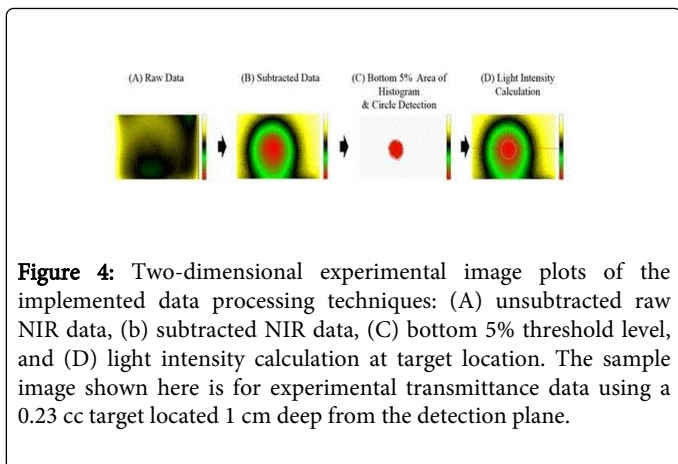
Figure 4: Two-dimensional experimental image plots of the implemented data processing techniques: (A) unsubtracted raw NIR data, (b) subtracted NIR data, (C) bottom 5% threshold level, and (D) light intensity calculation at target location. The sample image shown here is for experimental transmittance data using a 0.23 cc target located 1 cm deep from the detection plane.

Preliminary *In Vivo* Breast Imaging Studies

The ability of the non-contact hand-held NIROS to detect targets *in vivo* breast tissues was analyzed by performing studies on a healthy subject over 21 years of age (a university IRB approved study). The study was focused on determining the ability of the scanner to detect an absorption-contrasted 0.46 cc target located in the intra-mammary fold of the breast (placed superficially and non-invasively as shown in Figure 5) under various conditions (with/without pressure and target).

The subject was seated and the breast tissue was placed between two transparent acrylic parallel plates (Figure 5), to mimic the gold standard x-ray mammography approach. This allows tissue compression in order to reduce tissue thickness and also eliminate motion. CW-based NIR images were acquired in the transmittance mode at various pressures and with and without the target placement (to mimic tumor and no tumor cases).

The detection camera was located on top of the movable plate and the source was positioned in the opposite side (below the fixed bottom plate). The target was placed closer to the source and away from the detector, to maximize the depth of target detection from the detection place.

Transmittance NIR images were acquired with and without target when no pressure and maximum pressure (limited by subject's comfort level) was applied. The acquired NIR images were then subtracted via different configurations in order to study the effect of pressure and/or target detectability.

Except the subtraction technique, other data post-processing techniques (as described for phantom studies) were not applied for *in vivo* human subject studies. Table 2 describes the different experimental cases that were performed and analyzed.
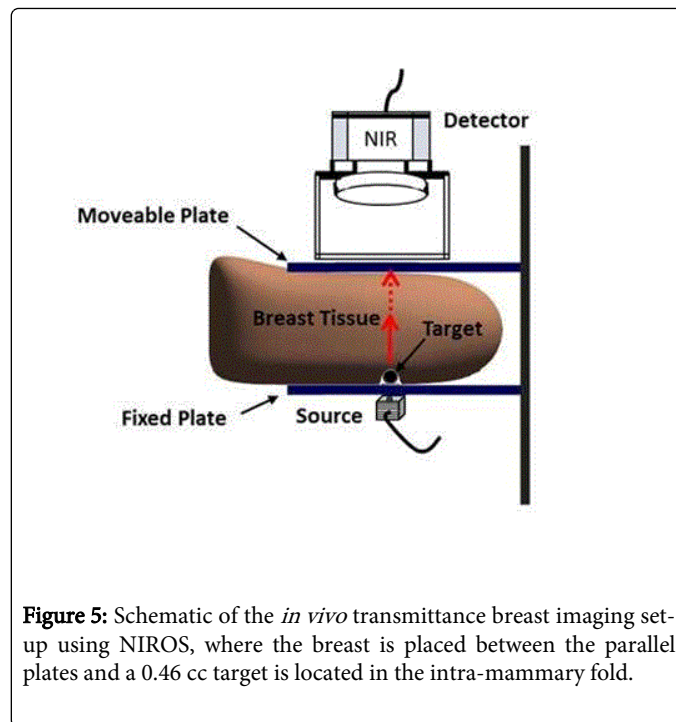
Figure 5: Schematic of the *in vivo* transmittance breast imaging set-up using NIROS, where the breast is placed between the parallel plates and a 0.46 cc target is located in the intra-mammary fold.

Case #	Target	Distance between Parallel Plane	Subtracted Images
1	0.46 cc (0.08% India Ink)	>6 cm	Target – Background (No pressure)
2	0.46 cc (0.08% India Ink)	>6 cm	Target – Background (Max pressure)
3	0.46 cc (0.08% India Ink)	>6 cm (with pressure)	Target with no pressure –Target with pressure
4	No target (Effect of pressure)	>6 cm (with pressure)	No target with no pressure – No target

Table 2: Quantitative analysis of detected target during transmittance imagingstudies performed using a 0.23 cc absorption target (~0.5 cm radius). The target was located at $[1.7 \times 1.6]$ cm in the x-y plane and at various depths ranging from 0.5 cm to 4 cm.

Results

The CW-based reflectance and transmittance NIR intensity images acquired using NIROS were processed in order to estimate target detectability at various target depths. The post-processed and subtracted NIR images for 8 different depth configurations (0.5 to 4 cm deep, at 0.5 cm increments) are shown in Figures 6 and 7 for reflectance and transmittance imaging studies, respectively. The preliminary *in vivo* breast imaging studies in transmittance mode are shown in Figure 8.

Reflectance Studies

Figure 6 shows the post-processed 2D NIR images from the reflectance imaging studies performed at various target depths. From these images, it can be observed that the 0.23 cc target was detected and differentiable from the background up to a depth of 2 cm. The

quantitative estimation of the detected target's centroid, its radius, distance between true and detected target location, and the target contrast are given in Table 3. Although the detected target's location is closer (≤0.55 cm) to the true location up to 4 cm deep (Table 3, last row), the contrast observed tends to reduce significantly beyond 1.5 cm deep. Quantitative analysis thus confirms that non-contact reflectance imaging using the current device is limited to 1.5 cm for targets as small as ~0.5 cm radius (of 0.23 cc volume). At 2 cm deep,

although the target appears to be detected from Figure 6, the RMS contrast (as well as contrast based on maximum difference) is too small to distinguish the target from background. The disadvantage of non-contact reflectance imaging for deep tissues is that the LED optical power is significantly reduced before it enters the tissue. This is because the source was placed far away from the detection surface (in order to illuminate the same 4×3 cm^2 detection area) causing greater attenuation of the source intensity.
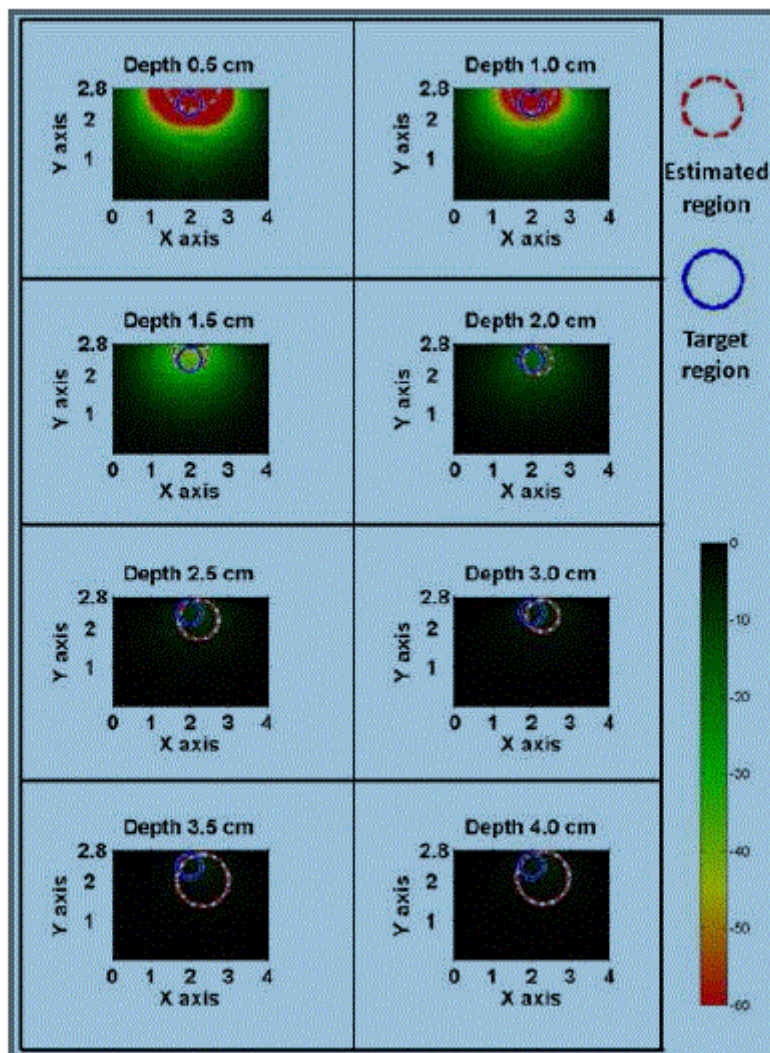
Figure 6: Two-dimensional subtracted NIR images obtained from reflectance studies performed using a ~0.5 cm radius (0.23 cc) spherical target filled at 0.8% India ink contrast. The true target (shown by solid blue circle) was located at [2.0 × 2.4] cm and at various depths of 0.5 to 4.0 cm in the cubical phantom (5.5 × 5.5 × 5.5 cm^3). The red-dotted hollow circle is the estimated target area, which is based on the 5% threshold of histogram.

Parameters		True Target Depth (cm)							
		0.5	1.0	1.5	2.0	2.5	3.0	3.5	4.0
Estimated Target (cm)	Centroid Location (cm)	[2.06, 2.95]	[2.00, 2.77]]	[2.02, 2.58]	[2.14, 2.39]	[2.22, 2.23]	[2.27, 2.33]	[1.67, 1.28]	[2.28, 2.10]
	Radius	0.70	0.58	0.44	.037	0.51	0.41	0.67	0.67
Contrast	Maximum Difference (level:0~255)	89	63	16	8	47	4	4	4
	RMS Contrast	9.92	6.04	3.28	1.52	0.61	0.44	0.29	0.31
Distance Off (cm)		0.55	0.36	0.17	0.14	0.28	0.29	0.49	0.42

Table 3: Quantitative analysis of detected target during reflectance imaging studies performed using a 0.23 cc absorption target (~0.5 cm radius). The target was located at [2.0 × 2.4] cm in the x-y plane and at various depths ranging from 0.5 cm to 4 cm.

Transmittance Studies

Figure 7 shows the post-processed 2D NIR images from the transmittance imaging studies performed at various target depths. From these images, it can be observed that the 0.23 cc target was detected and differentiable from the background across the entire depth of the phantom (i.e. 4 cm). The quantitative estimation of the detected target's details is given in Table 3. Both the RMS contrast and contrast based on maximum difference was consistently higher at all target depths of 0.5 to 4 cm unlike in reflectance imaging, where it dropped with target depth. This could be due to the loss of source intensity in the reflectance signal that affected deep target detectability and/or the further attenuation of the back-reflected light before it was detected at the surface. In comparison to the reflectance imaging studies, transmittance imaging provided the deepest target detection. In addition, the detected target location was closer to the true target location in all cases (≤0.35 cm). The distance off between the true and detected targets centroid increased at the target was moving away from the detected plane (and closer to the source plane).
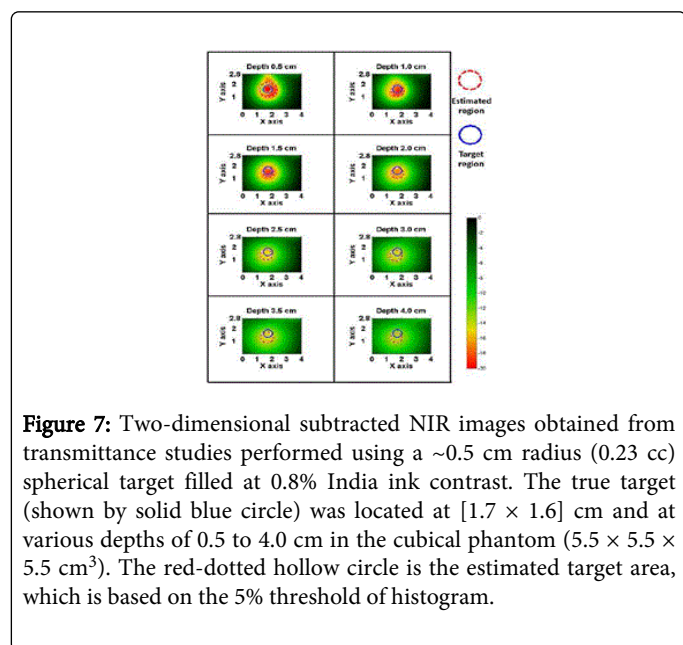
Figure 7: Two-dimensional subtracted NIR images obtained from transmittance studies performed using a ~0.5 cm radius (0.23 cc) spherical target filled at 0.8% India ink contrast. The true target (shown by solid blue circle) was located at [1.7 × 1.6] cm and at various depths of 0.5 to 4.0 cm in the cubical phantom (5.5 × 5.5 × 5.5 cm^3). The red-dotted hollow circle is the estimated target area, which is based on the 5% threshold of histogram.

Preliminary *in vivo* Transmittance Breast Imaging

Figure 8 shows the 2D surface NIR images of the breast tissue obtained from transmittance imaging with/without targets and with/without applied pressure. For each of the experimental case (#1-#4) described in Table 4, the 2D surface NIR images of the breast tissue (i) with target, (ii) without target (or background breast), (iii) subtracted (i.e. (i) – (ii)), and (iv) subtracted and plotted to scale across all 4 experimental cases, are shown in Figure 8. It can be observed across all the experimental cases that subtracted images (i.e. (iii)) show an area of higher absorption (blue), as marked by a white dotted line.

This differential absorption can be from the absorption contrasted-target (as in cases #1 and #2 from the 0.46 cc India ink target) and/or from decreased the blood flow due to increased pressure (as in cases #3 and #4), as observed from the 3rd column of Figure 8. The subtracted images were plotted to the same scale (4th column of images for all cases in Figure 8) in order to compare the differences (if any) in the absorption pattern due to the presence of a target and/or changes in pressure. In case #1, when there was an absorption-contrasted target with no pressure applied during imaging, the extent of changes in absorption is small (as observed from subtracted image in 3rd column), but appears insignificant when plotted to scale (i.e. 4th column image) with respect to other cases (#2- #4). This states that with no pressure of any sort applied, a 0.46 cc target is detectable but with a low contrast.

Upon applying pressure as in case #2 (that is, with and without target at maximum pressure), the region of increased absorption (blue) at the target site was distinct from the background with increased contrast over case #1. When the absorption contrasted target was present and only pressure was changed, as in case #3, the increased absorption due to changes in blood flow does not appear localized to the target site but spread over a large area (as observed form the subtracted images in 3rd and 4th column of case #3).

Interestingly, similar increased absorptions from changes in blood flow was observed spread over large areas when pressure was changed even without the presence of an absorption contrasted target (as in case #4). The increased absorption with increased pressure (up to comfortable levels) could be from increased blood flow in the breast tissue, causing an increase in total hemoglobin (one of the tissue absorbing components at NIR wavelengths).

Alternately, the 780 nm wavelength of light is close to the isosbestic point, the point at which the absorption spectra of oxy and de-oxy hemoglobin intersect [34]. Thus the higher absorption regions (due to the presence of tumors) represent the increased total hemoglobin concentrations (HbT), independent of the oxygen saturation content of hemoglobin. These preliminary results demonstrate that changes in absorption can be observed from both the presence of target and pressure changes.

However, the effect of only pressure changes (with or without a target as in cases #4 and 3, respectively) is observed as a spread out signal and not localized as observed from effect of target alone (as in cases #1 and 2).

Additionally, the distance between the two parallel plates was ~6 cm in the cases where pressure was applied. This states that an absorption-contrasted target as deep as 6 cm was detectable using the noncontact transmittance based NIROS.

Extensive studies will have to be carried out *in vivo* to develop appropriate metrics for target differentiation in breast tissues using various target sizes, depths and contrasts, prior to its application on breast cancer subjects. These extensive studies will also include imaging of normal breast tissues without any targets, in order to determine the best threshold values required in applying the thresholding technique to highly heterogeneous breast tissues.
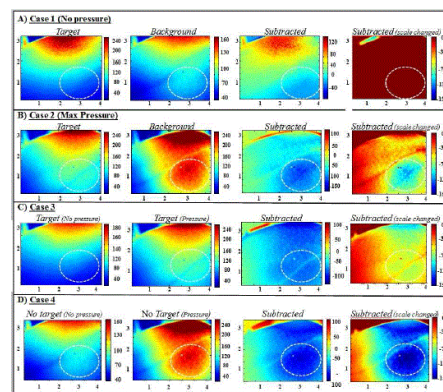
Figure 8: Surface contour plots of detected NIR images of *in vivo* breast tissue with a 0.46 cm^3 target located in the intra-mammary fold. a) Case #1 represents the case when no pressure is applied and images are acquired with and without a target in the background phantom. b) Case #2 is the same as case # 1 performed when maximum comfortable pressure was applied. c) Case #3 represents the case when images are acquired with maximum pressure and no pressure in a background phantom containing the target, and d) Case # 4 is the same as Case # 3, except that the images are acquired performed in a phantom containing no target. The white dotted circle shows the area of interest. The last column is the subtracted images plotted to scale across cases #1-4.

Parameters		True Target Depth (cm)							
		0.5	**1.0**	**1.5**	**2.0**	**2.5**	**3.0**	**3.5**	**4.0**
Estimated Target (cm)	**Centroid Location (cm)**	[1.75, 1.56]	[1.73, 1.47]	[1.76, 1.44]	[1.70, 1.40]	[1.61, 1.37]	[1.60, 1.32]	[1.67, 1.28]	[1.65, 1.26]
Contrast	**Radius**	0.59	0.43	0.39	0.42	0.40	0.42	0.42	0.38
	Maximum Difference (level:0~255)	104	59	58	52	47	45	46	43
	RMS Contrast	22.55	21.18	23.24	23.24	22.49	23.10	25.50	25.04
Distance Off (cm)		0.05	0.14	0.18	0.20	0.26	0.31	0.33	0.35

Table 4: Details of the experimental cases for *in vivo* breast imaging studies using NIROS.

Discussion and Conclusion

In the present work, a hand-held fiber-free non-contact near-infrared optical scanner (NIROS) has been developed that is capable of both reflectance as well as transmittance imaging using LED-based sources and CCD-based detector. Since the device does not use optical fibers for launching or collecting the NIR signals from the phantom/tissue surface, the NIR optical data avoids issues common to optical fiber based systems. Here in, phantom studies were performed under reflectance and transmittance modes using targets at various depths (0.5 to 4 cm deep). With the use of various data post-processing approaches (median filtering, thresholding, and subtraction technique), targets were detected >1cm even in the reflectance mode,

while all the past studies were limited to ≤1 cm using either reflectance or transmittance mode. While targets were detected up to 1.5 deep in reflectance mode, they were detected across the entire depth of the phantom (i.e. 4 cm deep) in transmittance mode. It is well known that transmittance imaging offers greater target depth detection (when using an optical-fiber based or no-fiber based NIR device) as also observed in the current study. These absorption-based phantom studies have demonstrated that the non-contact hand-held NIROS has applicability as a reflectance-based device for subsurface monitoring of peripheral blood flow changes; and as a transmittance-based device for deep target detections (e.g. breast cancer). The preliminary *in vivo* studies on the normal breast tissues with a superficially placed target in the intra-mammary fold have shown that an increased absorption was

clearly observed from the target site (~6 cm deep) when (maximum comfortable) pressure was applied. In an actual breast cancer case, this may translate to imaging the contralateral breast and comparing the differences in the absorption across the two tissues, via symmetric clock-wise imaging of the breast (as in an ultrasound approach). Currently, work is carried out to image both the left and right breast tissues and compare the two, as there are structural differences between the two. These structural differences can lead to differences in NIR images (from physiological differences). Hence, understanding the hemodynamic differences between normal left and right breasts can help differentiate between the breast abnormalities with respect to the contralateral breast (acting as a reference) in the future.

In parallel, a miniature positional tracking system is developed and implemented on the handheld NIROS in order to accurately determine the location of the imaged region with respect to the entire breast tissue. This positional tracking system can also assist in avoiding operator dependency errors during bilateral symmetric breast imaging studies, and/or repeated studies during subsequent visits by the subjects. Apart from reflectance and transmittance imaging, NIROS is also capable of performing adjacent imaging, wherein the source and the detector could be placed across adjacent surfaces during imaging. While the reflectance/transmittance imaging can provide tentative 2D location of the detected target, adjacent imaging may provide the 3rd dimension of the target (as observed from out past studies) [35]. There are ongoing efforts to perform extensive *in vivo* studies under various experimental conditions to determine the capabilities of the non-contact hand-held NIROS in detecting smaller and deeper targets. A 2010 U.S study conducted by the Medco Research Institute revealed that only half of the insured women over the age of 40 are claiming annual mammogram screenings, despite medical recommendations endorsed across the US and the world [36,37]. Reasons for noncompliance suggested from various studies include discomfort during the exam, concern over radiation exposure, access to facilities, inconvenience/lack of time, embarrassment/cultural barriers, and denial. Thus, to improve breast cancer screening compliance, a need exists for a safe, comfortable, accessible, and convenient breast cancer pre-screening tool to better triage the subjects for early detections/treatment options. There is a potential for a functional imaging tool to provide additional information to the clinical or self-breast examinations at the pre-screening stage that may provide more information to the clinicians. Although the hand-held non-contact NIROS cannot determine the accurate location of a target, as other 3D tomography based optical imagers, it may have the potential to detect the presence of any abnormalities (or target(s)) as an initial assessment to breast pre-screening. The ability to perform deep tissue imaging using a portable hand-held NIROS allows for *in vivo* breast studies. Following the extensive *in vivo* studies on normal subjects, studies will be performed on breast cancer subjects to validate the above stated hypothesis and determine the capabilities of the device for breast cancer prescreening. In this effort, NIROS is currently modified to allow hemodynamic imaging (using a dual wavelength source system) such that the changes in oxy and deoxy-hemoglobin from breast tissues can be determined apart from changes in absorption alone.

Acknowledgements

References

1. Colak SB, van der Mark MB, Hooft GW, Hoogenraad JH, van der Linden ES, et al. (1999) Clinical optical tomography and NIR spectroscopy for breast cancer detection. IEEE J Sel Top Quantum Electron 5: 1143-1158.

2. Leff DR, Warren OJ, Enfield LC, Gibson A, Athanasiou T, et al. (2008) Diffuse optical imaging of the healthy and diseased breast: a systematic review. Breast Cancer Res Treat 108: 9-22.

3. Gibson AP, Hebden JC, Arridge SR (2005) Recent advances in diffuse optical imaging. Phys Med Biol 50: R1-43.

4. Gonzalez J, Decerce J, Erickson SJ, Martinez SL, Nunez A, et al. (2012) Hand-held optical imager (Gen-2): improved instrumentation and target detectability. J Biomed Opt 17: 081402-081401.

5. Devices for breast cancer: spectroscopic and 3D tomographic imaging. IEEE J Sel Top Quantum Electron 18: 1298-1312.

6. Erickson SJ, Godavarty A (2009) Hand-held based near-infrared optical imaging devices: a review. Med Eng Phys 31: 495-509.

7. Fang Q, Carp SA, Selb J, Boverman G, Zhang Q, et al. (2009) Combined optical imaging and mammography of the healthy breast: optical contrast derived from breast structure and compression. IEEE Trans Med Imaging 28: 30-42.

8. Culver JP, Choe R, Holboke MJ, Zubkov L, Durduran T, et al. (2003) Three-dimensional diffuse optical tomography in the parallel plane transmission geometry: evaluation of a hybrid frequency domain/continuous wave clinical system for breast imaging. Med Phys 30: 235-247.

9. Palmer MR, Shibata Y, Kruskal JB, Lenkinski RE (2002) In vivo imaging of small animals with optical tomography and near infrared fluorescent probes. Proceedings of the SPIE.

10. Wieringa FP, Mastik F, Ten Cate FJ, Neumann HAM, van der Steen AFW (2006) Remote noninvasive stereoscopic imaging of blood vessels: First in-vivo results of a new multispectral contrast enhancement technology. Ann Biomed Eng 34: 1870-1878.

11. Han X, Lui H, McLean DI, Zeng H (2006) A technique for near-infrared autofluorescence imaging of skin: preliminary results. Proceedings of the SPIE.

12. Matsushita T, Miyati T, Nakayama K, Hamaguchi T, Hayakawa Y, et al. (2011) Qualitative near-infrared vascular imaging system with tuned aperture computed tomography. J Biomed Opt 16: 076004.

13. Han X, Lui H, McLean DI, Zeng H (2009) Near-infrared autofluorescence imaging of cutaneous melanins and human skin in vivo. J Biomed Opt 14: 024017.

14. Abookasis D1, Lay CC, Mathews MS, Linskey ME, Frostig RD, et al. (2009) Imaging cortical absorption, scattering, and hemodynamic response during ischemic stroke using spatially modulated near-infrared illumination. J Biomed Opt 14: 024033.

15. Bouzida N, Bendada AH, Maldague XP (2010) Near-infrared image formation and processing for the extraction of hand veins. J Mod Opt 57:1731-1737.

16. Mizuno Y, Katayama T, Nakamachi E (2010) Development of an accurate 3D blood vessel searching system using NIR light. Proceedings of the SPIE.

17. Lee BT, Matsui A, Hutteman M, Lin SJ, Winer JH, et al. (2010) Intraoperative near-infrared fluorescence imaging in perforator flap reconstruction: current research and early clinical experience. J Reconstr Microsurg 26: 59-65.

18. Chen P, Chang M, Chiu F, Li C, Law AB-L (2010) Quantitative measurements of blood vessel of diabetic extremity based on near-infrared image technique. Proceedings of the 6th World Congr Biomech.

19. Jakovels D, Spigulis J (2010) 2-D mapping of skin chromophores in the spectral range 500 - 700 nm. J Biophotonics 3: 125-129.

20. Shao X, Zheng W, Huang Z (2010) Polarized near-infrared autofluorescence imaging combined with near-infrared diffuse reflectance imaging for improving colonic cancer detection. Opt Express 18: 24293-24300.

21. Shimawaki S, Sakai N (2010) Change in blood vessel images of the human finger using near infraredradiation while compressing the upper arm. Proceedings of the World Congr Biomech.

22. Matsushita T, Miyati T, Nakayama K, Hamaguchi T, Hayakawa Y, et al. (2011) Qualitative near-infrared vascular imaging system with tuned aperture computed tomography. J Biomed Opt 16: 076004.

23. Lin ZJ, Niu H, Liu Y, Su J, Liu H (2011) CCD-camera-based diffuse optical tomography to study ischemic stroke in pre-clinical rat models. Proceedings of SPIE.

24. Liu Y, Bauer AQ, Akers WJ, Sudlow G, Liang K, et al. (2011) Hands-free, wireless goggles for near-infrared fluorescence and real-time image-guided surgery. Surgery 149: 689-698.

25. Mieog JS, Troyan SL, Hutteman M, Donohoe KJ, van der Vorst JR, et al. (2011) Toward optimization of imaging system and lymphatic tracer for near-infrared fluorescent sentinel lymph node mapping in breast cancer. Ann Surg Oncol 18: 2483-2491.

26. Mieog JS, Hutteman M, van der Vorst JR, Kuppen PJ, Que I, et al. (2011) Image-guided tumor resection using real-time near-infrared fluorescence in a syngeneic rat model of primary breast cancer. Breast Cancer Res Treat 128: 679-689.

27. Kuzmina I, Diebele I, Jakovels D, Spigulis J, Valeine L, et al. (2011) Towards noncontact skin melanoma selection by multispectral imaging analysis. J Biomed Opt 16: 060502.

28. Osaki R, Ding M, Hyodo H, Soga K, Takemura H, et al. (2011) 3D bioimaging sensor of breast cancer cell using rare-earth-doped ceramic nanophosphors and near-infrared. Proceedings of the IEEE Sensors.

29. Arce GR (2005) Nonlinear Signal Processing: A Statistical Approach. Wiley, New Jersey, USA.

30. Sezgin M, Sankur B (2004) Survey over image thresholding techniques and quantitative performance evaluation. J Electron Imaging 13: 146-165.

31. Ridler T, Calvard S (1978) Picture thresholding using an iterative selection method. IEEE Trans Syst Man Cybern 8: 630-632.

32. Otsu N (1979) A threshold selection method from gray-level histograms. IEEE Trans Syst Man Cybern 9: 62-66.

33. Anjos AD, Shahbazkia H (2008) Bi-level image thresholding - A fast method. Biosignals 2: 70-76.

34. Peli E (1990) Contrast in complex images. J Opt Soc Am A 7: 2032-2040.

35. Chance B, Leigh JS, Miyake H, Smith DS, Nioka S, et al. (1988) Comparison of time-resolved and -unresolved measurements of deoxyhemoglobin in brain. Proc Natl Acad Sci U S A 85: 4971-4975.

36. Ge J, Erickson SJ, Godavarty A (2010) Multi-projection fluorescence optical tomography using a handheld-probe-based optical imager: phantom studies. Appl Opt 49: 4343-4354.

37. Wall M, McDermott MP, Kieburtz KD, Corbett JJ, Feldon SE, et al. (2014) NORDIC Idiopathic Intracranial Hypertension Study Group Writing Committee, Effect of acetazolamide on visual function in patients with idiopathic intracranial hypertension and mild visual loss: the idiopathic intracranial hypertension treatment trial. JAMA 311: 1641-1651.